The Astrophysical Journal, 711:125–137, 2010 March 1 doi:10.1088/0004-637X/711/1/125

SYNCHROTRON EMISSION FROM ELLIPTICAL GALAXIES CONSEQUENT TO ACTIVE GALACTIC NUCLEUS OUTBURSTS

Yan-Fei Jiang[1], Luca Ciotti[2], Jeremiah P. Ostriker[1,3], and Anatoly Spitkovsky[1]
[1] Department of Astrophysical Sciences, Princeton University, NJ 08544, USA
[2] Department of Astronomy, University of Bologna, via Ranzani 1, I-40127 Bologna, Italy
[3] IoA, Cambridge, UK
Received 2009 April 29; accepted 2010 January 15; published 2010 February 8

ABSTRACT

Both radiative and mechanical feedback from active galactic nuclei have been found to be important for the evolution of elliptical galaxies. We compute how a shock may be driven from a central black hole into the gaseous envelope of an elliptical galaxy by such feedback (in the form of nuclear winds) using high resolution one-dimensional hydrodynamic simulations. We calculate the synchrotron emission from the electron cosmic rays accelerated by the shocks (not the jets) in the central part of elliptical galaxies, and we also study the synchrotron spectrum's evolution using the standard diffusive shock acceleration mechanism, which is routinely applied to supernova remnants. We find quantitative consistency between the synchrotron radio emission produced via this mechanism with extant observations of elliptical galaxies which are undergoing outbursts. Additionally, we also find that synchrotron optical and X-ray emission can co-exist inside elliptical galaxies during a specific evolutionary phase subsequent to central outbursts. In fact, our calculations predict a peak synchrotron luminosity of $\sim 1.3 \times 10^6\ L_\odot$ at the frequency 5 GHz (radio band), of $\sim 1.1 \times 10^6\ L_\odot$ at 4.3×10^{14} Hz (corresponding to the absolute magnitude −10.4 in *R* band), and of $\sim 1.5 \times 10^7\ L_\odot$ at 2.4×10^{17} Hz (soft X-ray, 0.5–2.0 keV band).

Key words: cosmic rays – galaxies: ISM – ISM: jets and outflows – radiation mechanisms: non-thermal – radio continuum: galaxies

Online-only material: color figures

1. INTRODUCTION

Is there direct evidence for feedback from active galactic nuclei (hereafter AGNs) available from the non-thermal emission of the central regions of massive galaxies? It has been observed that 10%–20% of AGNs are radio loud and that the host galaxies of radio-loud AGNs are usually massive elliptical galaxies (e.g., Hooper et al. 1995; Best 2007). The radio emission in radio galaxies and quasars comes from a variety of morphological structures, with different characteristic sizes. For example, there are compact radio cores (usually with flat power-law spectra) coincident with the nucleus of the associated optical objects, as well as large scale radio lobes. Other systems show radio lobes which may extend to several hundred kiloparsecs to a few megaparsecs and usually show steep power-law radio spectra (e.g., Kellermann et al. 1994; Krolik 1999; Kembhaavi & Narlikar 1999; Gilbert et al. 2004; Mullin et al. 2006). The typical core radio luminosity for FR-II sources at 5 GHz is $\sim 10^{30}$ erg s^{-1} Hz^{-1}, while the total luminosity at 178 MHz is $\sim 10^{33}$ erg s^{-1} Hz^{-1} (e.g., Chiaberge et al. 2000), with the spectral index (absolute value) typically smaller than 0.5 at the very center and ∼0.7–0.8 at a larger radius. In addition to the radio observations, there are also observations in other bands for radio galaxies. For example, in the *R*-band 3CR Snapshot Survey of 252 radio galaxies, the wind-like structures seen in the contour figures of Martel et al. (1999) may be interpreted as produced by nuclear winds. Kiloparsec-scale winds are also observed in high redshift quasars (e.g., de Kool et al. 2001; Nesvadba 2009; Nesvadba et al. 2008; Moe et al. 2009; Cattaneo et al. 2009 and references therein). Optical synchrotron jets are also confirmed in many sources (e.g., Martel et al. 1999) and can extend to distances far outside of the body of the galaxies. Furthermore, ultraviolet and X-ray observations have also found high-velocity outflows in some quasars (e.g., Nesvadba et al. 2008; Hamann et al. 2008; Nesvadba 2009; Alexander et al. 2010; Chartas et al. 2009). Finally, although the evidence is not absolutely conclusive, there are observations (e.g., Chiaberge et al. 2000) indicating optical synchrotron from the cores of some active elliptical galaxies. The obvious question is "what processes accelerate cosmic ray (hereafter CR) electrons up to the energies required to produce the observed synchrotron emission?"

Synchrotron emission is believed to be the mechanism responsible for the radio emission in AGNs, based on their strong polarization (e.g., Krolik 1999). The relativistic electrons, which are required for the synchrotron radio emission, can be accelerated by several sources. Jets are observed in most of the radio-loud AGNs and most investigators believe that those jets produce this radio synchrotron emission (e.g., Rees 1971; Blandford & Rees 1974; Sironi & Socrates 2010; also see the review Mirabel & Rodríguez 1999 and references therein). However, the energy carried by the jets is only dissipated in small areas near the endpoint or within internal reflected shocks. As the jets are driven outward with relativistic velocity, the centers of the radio contours from the jets do not overlap with the centers of the galaxies (see, e.g., Kellermann et al. 1994; Mullin et al. 2006). So, although jets are very likely responsible for the displaced radio lobes, there must be other mechanisms responsible for the observed radio core emission at the centers of FR-II galaxies. Furthermore, in order to explain synchrotron emission in galaxies without jets, other sources able to accelerate electrons are needed. In fact, jets are observed in ∼80% of FR-I radio galaxies, in ∼40%–70% radio quasars, and even fewer in highly luminous FR-II galaxies (e.g., Bridle & Perley 1984; Kembhaavi & Narlikar 1999).

This paper addresses the inevitable generation of radio synchrotron sources in elliptical galaxies consequent to central outbursts. In fact, it is now widely accepted that supermassive black holes (SMBHs) within a mass range of 10^6–$10^{9.5}$ $M_\odot$ reside at the center of bulges and elliptical galaxies, and that feedback from these SMBHs can profoundly affect the formation and evolution of these galaxies (e.g., Kormendy & Richstone 1995; Silk & Rees 1998; Fabian 1999; Burkert & Silk 2001; King 2003; Granato et al. 2004; Springel et al. 2005; Sazonov et al. 2005; Hopkins et al. 2006; Hu et al. 2006). This is strongly supported by the observed relationships between the masses of the SMBHs and various properties of their host galaxies (e.g., Magorrian et al. 1998; Gebhardt et al. 2000; Ferrarese & Merritt 2000; Tremaine et al. 2002; McLure & Dunlop 2002; Graham & Driver 2007; Lauer et al. 2007; Lou & Jiang 2008). In particular, in a series of works based on high resolution numerical simulations which include both radiative and mechanical feedback (Ciotti & Ostriker 1997, 2001, 2007; Ciotti et al. 2009b, hereafter Paper I), it has been shown how the mass loss from evolving stars can drive significant nuclear activity, characterized by strong and recurrent nuclear bursts, even in the absence of merging. This model supports the idea that the "cooling flow" phases (e.g., Peterson & Fabian 2006) and quasar phases are different aspects of the evolution of a normal elliptical galaxy. In the calculations, it is found that accretion occurs in bursts, during which both radiative and mechanical output from the central SMBH pushes matter out and drives shocks into the galactic gas. The outbursts typically combine three physically separate phenomena: central star bursts, mechanical feedback from winds emanating from broad-line regions surrounding the SMBH, and radiative feedback from absorption and scattering of hard X-ray photons. The resulting shocks are similar in kind (but more modest in degree) to the predicted outflowing blast waves produced by AGNs after galaxy merging (e.g., see Di Matteo et al. 2005; Springel et al. 2005; Naab et al. 2006; Sijacki et al. 2007; also see Johansson et al. 2009). A similar idea to ours is also applied to galaxy clusters (e.g., Fujita et al. 2007).

In this paper, we focus attention on the observational properties of the emitted synchrotron emission from the shocks that result from the recurrent bursts. In fact, since the computed outflow velocities (up to several thousand kilometers per second) and densities (0.1–10 particles per cubic centimeter) are similar to what is observed in Galactic supernova remnants (SNRs), such as Tycho and Kepler (e.g., Cassam-Chenaï et al. 2007; Dickel et al. 1988), one would expect that the same processes as those we see acting in SNRs on the parsec scale (specifically at the shocks' surfaces; Wang 2008) would act on the kiloparsec scale in galaxies. One can expect there to be efficient acceleration of both ionic and electronic CRs via the well known diffusive shock acceleration mechanism (also known as first-order Fermi shock acceleration, e.g., Blandford & Ostriker 1978; Blandford & Eichler 1987; Berezhko & Ellison 1999; also see Treumann & Jaroschek 2008). Then, just as the accelerated CR electrons produce synchrotron emission through standard interactions with the (possibly amplified) magnetic field within normal SNRs, so we should expect very similar processes to occur in the ISM of elliptical galaxies after outbursts. To our knowledge, this has not yet been studied in quantitative detail. Using diffusive shock acceleration theory, we can make a rough estimate of the scaling relation for luminosity, because the synchrotron luminosity only depends on the CR electron density, the magnetic field B, and the shock velocity. If the density and velocity of the shock are fixed, the luminosity is determined by the volume occupied by CR electrons and the magnetic field. The extent of emitting region near the shock is determined by the synchrotron losses of the electrons, which are proportional to B^2, so that the volume occupied by CR electrons goes with r^2/B^2 (r is the radius of the shock). Because power per volume radiated by the electrons goes like B^2, the total luminosity scales approximately as r^2. As the size of an elliptical galaxy is $\sim$100 times larger than the SNRs, and the densities and shock velocities in the cores of elliptical galaxies are expected to be very similar to those in SNRs, we expect the synchrotron luminosity from elliptical galaxy cores to be $\sim 10^4$–10^5 larger than the luminosity from SNRs. Our detailed calculations (see Section 3) confirm these rough scaling estimates.

In this paper, we calculate synchrotron emission from the relativistic electrons accelerated by shocks during the evolution of an elliptical galaxy and we also show how the synchrotron spectrum evolves with time. The Ciotti & Ostriker model for the evolution of elliptical galaxies provides us with a specific scenario for computing the shocks, which are formed repeatedly due to the feedback of the central SMBHs. With the propagation of the shock into the interstellar medium (ISM), electrons will be accelerated at different positions (via the standard diffusive shock acceleration mechanism), and high-energy particles can be found at large radii. This is very different from the concept which sometimes proposed that CRs are accelerated at the center and escape to large radius, since such CR electrons would suffer from large adiabatic losses and become relatively ineffective radiators. In Section 2, we present the method to calculate the accelerated electron spectrum and associated synchrotron emission. In Section 3, we show the result from a single shock taken from a numerical simulation. The main results are summarized in Section 4, and discussions and observational results of our model are given in Section 5.

2. CALCULATION METHOD

In this section, we describe the numerical model adopted for the simulation and we give the formulae for the diffusive shock acceleration mechanism and synchrotron emission used in this paper.

2.1. *The Hydrodynamic Model*

The details of hydrodynamic simulations of radiative plus mechanical feedback and how the kinetic energy, momentum, and mass of the wind are transferred to the ISM in combined (i.e., radiative plus mechanical feedback) models are described in Paper I, while the exploration of parameter space in combined models is postponed to (L. Ciotti et al. 2010, in preparation, hereafter Paper III). We recall that the code is one-dimensional (1D), and that, as in Paper I, a simplified version of mechanical feedback is adopted,[4] which is similar to that used by others (e.g., Di Matteo et al. 2005) studying AGN feedback. The galaxy model is a Jaffe stellar distribution embedded in a dark halo so that the total density profile decreases as r^{-2} (Ciotti et al. 2009a and references therein). The cooling and heating functions (Sazonov et al. 2005) include photoionization plus Compton and line heating, while the SMBH accretion rate is mediated by a circumnuclear accretion disk modelized at the level of subgrid physics. Finally, the mass return rate from evolving stellar populations is computed by using the detailed prescriptions of stellar evolution. A discussion of the limitations of 1D simulation is deferred to Section 4.

---

[4] In practice, the time derivative in Equation (28) of Paper I is set to zero.

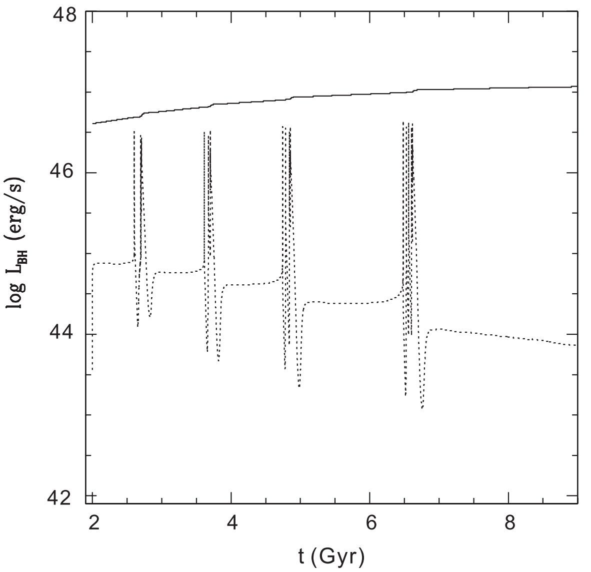

Figure 1. Time evolution of the SMBH bolometric accretion luminosity $L_{\rm BH}$ for model B3$_{02}$. The nearly horizontal solid line is the Eddington luminosity $L_{\rm Edd}$. There are four major bursts during the evolution history of the model, and each major burst is composed of several sub-bursts.

In the following discussion, we focus on a specific model labeled B3$_{02}$ (Paper I; Paper III), which models the radiation and mechanical feedback from AGNs to the host elliptical galaxies. This model has an initial stellar mass $M_\star = 2.87 \times 10^{11}\, M_\odot$ and an initial SMBH mass $M_{\rm BH} = 2.87 \times 10^8\, M_\odot$. The galaxy effective radius is $R_{\rm e} = 6.9$ kpc and the aperture central velocity dispersion is $\sigma_0 = 260$ km s^{-1}. The first grid point in the code corresponds to $R_{\rm min} = 5$ pc. The simulation starts at 2 Gyr and lasts to 14.5 Gyr. The time evolution of the SMBH bolometric accretion luminosity is shown in Figure 1.

The computations show that a cooling instability (Field 1965) starts as a cool ($T \sim 10^4$ K) and dense shell at $r \sim 1$ kpc; this shell collapses, feeds gas into the center, and the SMBH responds with a major burst. In more detail, the infalling shell compresses the gas inside the collapsing volume, so that more and more gas is accreted by the SMBH even before the cold shell reaches the center. The luminosity of SMBH increases rapidly with time, and when it reaches ~1% of Eddington luminosity, the infalling matter is pushed out by the radiation from the SMBH (e.g., Ostriker et al. 1976; Milosavljević et al. 2009). At the same time, a wind appears from the circumnuclear disk and a shock is driven into the ISM. The shock hits the still infalling cold shell at a very high Mach number, due to the low temperature of the shell. The shock continues to propagate into the galaxy; gradually its energy is deposited into the ISM, and it dies away with time. In the meantime, reverse shock waves carry fresh gas to the center, and several sub-bursts are generated. Finally, the last burst ends the sequence. The duty cycle—the fraction of time that the central SMBH is in the outburst mode with $L_{\rm BH} > L_{\rm Edd}/30$—is of the order of ~5%, consistent with the fraction of elliptical galaxies seen as quasars. As commonly found in combined (i.e., radiative plus mechanical feedback) models discussed in full extent in Paper III, the temporal structure of each major burst is highly organized into a series of sub-bursts (as apparent from the temporal structure of each of the four major bursts in Figure 1), while purely mechanical feedback models present much simpler bursts, as can be seen by comparison with Figures 2–4 in Paper I. In our case, each shock will accelerate electrons and protons.

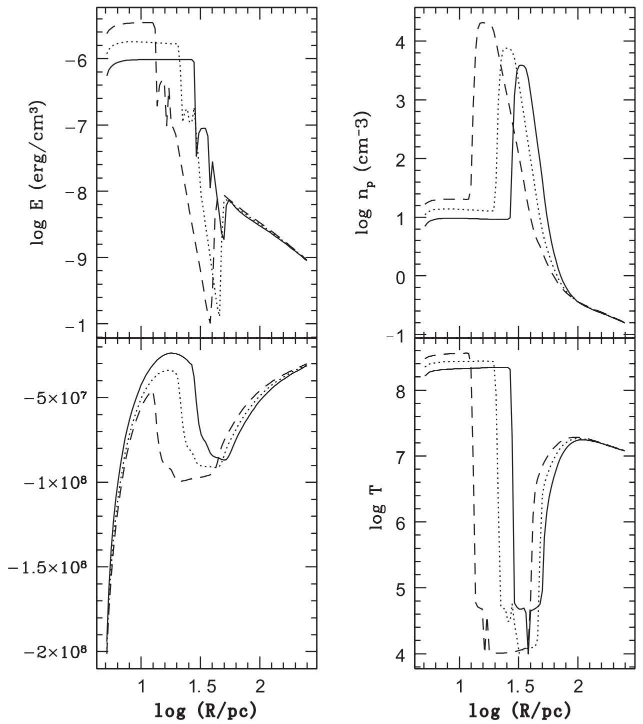

Figure 2. Thermal instability and the falling cold shell: the radial profile of the ISM energy per unit volume E, proton number density n_p, radial velocity v, and temperature T. Solid, dotted, and dashed lines correspond to $\Delta t = 0.204$, 0.214, and 0.224 Myr after $L_{\rm BH}$ reached 0.01 $L_{\rm Edd}$ (6.48 Gyr, see Figure 1). This time is defined to be the zero point. Note how the gas density in the central regions increases due to compression before the cold shell (40 pc from the center at $\Delta t = 0.204$ Myr) reaches the center.

Now we focus on the first sub-burst in the last major burst around 6.5 Gyr. The SMBH bolometric accretion luminosity $L_{\rm BH}$ reaches 1% of Eddington luminosity $L_{\rm Edd}$ at the time 6.48 Gyr, and we define this time as the zero time point. With this time origin, $L_{\rm BH}$ reaches 0.1 $L_{\rm Edd}$ around 0.234 Myr later, and it peaks at 0.5$L_{\rm Edd}$ at $\Delta t = 0.252$ Myr. Figure 2 shows the radial profile of the physical variables at $\Delta t = 0.204$ Myr, just before the peak of the burst. We can clearly see the cold shell initially at 40 pc falling to the center. Figure 3 shows the appearance of outflow with the solid line ($\Delta t = 0.235$ Myr) still before the peak of the burst: the wind pushed out by radiation from the SMBH reaches 5.1 pc, with a velocity of only 100 km s^{-1} (arrow A). By the time the shock reaches 15 pc (arrow B), the maximum velocity has increased up to 3600 km s^{-1}, as it is being steadily accelerated from below, and it has hit the infalling cold shell, which results in a very high Mach number shock.

2.2. *Acceleration of Particles at the Shocks*

Synchrotron emission from shocks based on the diffusive acceleration mechanism has been applied to astrophysical systems on different scales. In particular, for SNRs there exist different non-linear models for the structure and evolution of CR-modified (strong) shocks (e.g., see Koyama et al. 1995; Berezhko & Ellison 1999; Ellison et al. 2000, 2004, 2007; Lazendic et al. 2004; Berezhko & Völk 2006; see the reviews by Reynolds 2008, Treumann & Jaroschek 2008). With this method, the synchrotron spectra at different radii and their evolution with time can be computed and then compared with the observations of SNRs, showing good agreement (e.g., Reynolds 1998; Lazendic et al. 2004; Cassam-Chenaï et al. 2007). Some researchers have also carried out simulations on the scale of

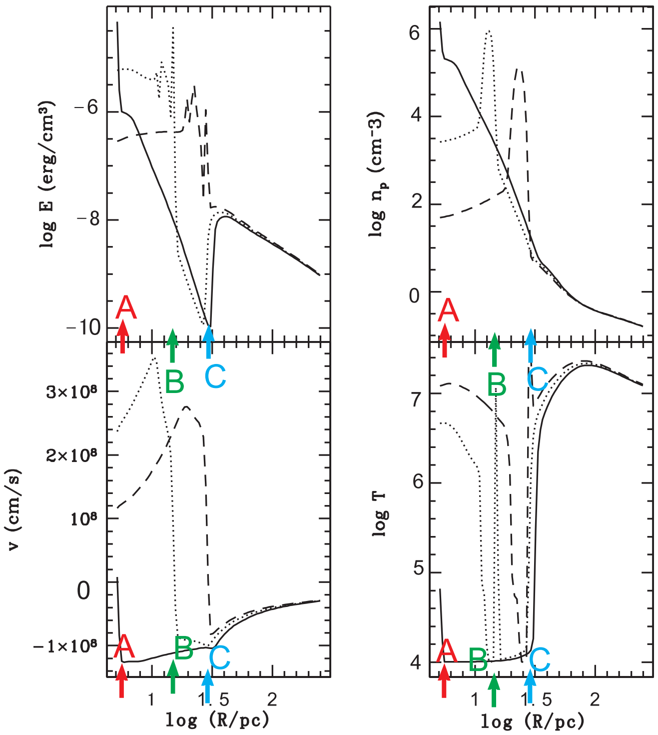

Figure 3. Post outburst: radial profile of the physical variables when a burst appears at $\Delta t_1 = 0.235$ Myr. Solid, dotted, and dashed lines correspond to $\Delta t = 0.235,\ 0.239$, and 0.243 Myr. The fluid radial velocity changes direction from inward to outward between $\Delta t_1 = 0.235$ Myr and $\Delta t_2 = 0.239$ Myr. The cold shell is still visible in the solid line at the center. The arrows (A, B, C) indicate the positions of the shock at the three defined moments (see Figure 4); the shock initially accelerates (A→B) due to the SMBH driving from below and then decelerates (B→C) as adiabatic losses overcome the SMBH input.

(A color version of this figure is available in the online journal.)

galaxy clusters to study the radio halos and relics based on the diffusive shock acceleration mechanism in the limit of test particle theory (e.g., Enßlin et al. 2007; Pfrommer et al. 2008). Here, we apply the same techniques to the case of wind-driven shocks in elliptical galaxies.

Our CR shock acceleration scheme is based on well established physical principles (the first-order Fermi mechanism) but utilizes a new, quite efficient numerical implementation, which allows us to perform the analysis during post-processing instead of during the runs, saving considerable computational time. We use the test particle theory to calculate the electron spectrum at the shock, which gives the basic characteristics of the non-thermal electrons (e.g., Blandford & Ostriker 1978; Blandford & Eichler 1987; also see the recent review by Reynolds 2008). Consistent with test particle theory, the CRs are assumed to not change the structure of the shocks, so that we can use the output of the hydrodynamic code to calculate the synchrotron spectrum.

In order to compute the acceleration of the electrons and protons, first we have to identify and follow the shocks as they move through the ISM. Each shock is driven by the combined effect of radiation and nuclear winds following a burst, and it propagates into the ambient gas of the elliptical galaxy. For each hydrodynamic output file, we calculate the dimensionless compression factor

$$\delta \equiv \frac{r}{|v_r|}\mathrm{div}(\mathbf{v}) \qquad (1)$$

at every point on the grid. Here, r is the radius, $\mathbf{v}$ is the fluid velocity vector, and $|v_r|$ is the absolute value of velocity.[5] As the shock strongly compresses the gas, a local deep minimum of δ marks the position of the shock. The upstream sonic Mach number of the shock is given by

$$\mathcal{M} = \frac{|v - u_s|}{c_s}, \qquad (2)$$

where u_s is the shock velocity relative to the galaxy and c_s is the upstream sound speed. The shock velocity u_s is numerically estimated by determining the change in the shock position within a time step. The upstream sound speed is calculated from the upstream temperature T and density ρ as

$$c_s = \sqrt{\left(\frac{\partial P}{\partial \rho}\right)_S} = \sqrt{\frac{\gamma k_B T}{\mu m_p}}, \qquad (3)$$

where P is the pressure, k_B is the Boltzmann constant, $\mu \cong 0.62$ is the mean molecular weight, m_p is the proton mass, and $\gamma = 5/3$ is the adiabatic index of the gas.

As the magnetic field B, necessary for the synchrotron emission, is not included in our hydrodynamic code, we must assume a fiducial value based on physical arguments. In particular, for elliptical galaxies, there is evidence that the ratio between the non-thermal and thermal pressures is about 0.1–0.2 (e.g., Churazov et al. 2008; E. Churazov et al. 2010, in preparation, private communication). Here, we just assume the ratio between the thermal and magnetic pressure to be

$$\beta \equiv \frac{P}{B^2/(8\pi)} \cong 10, \qquad (4)$$

so that we can estimate the postshock magnetic field from the thermal pressure.

Now we summarize the basic results of the test particle theory. The 1D momentum spectrum of the non-thermal electrons is taken to be a power law:

$$f(p) = 4\pi p^2 \times \mathcal{C}_0\ p^{-q} = 4\pi \mathcal{C}_0\ p^{2-q}, \qquad (5)$$

where p is the momentum of the electrons and $\mathcal{C}_0$ is the normalization of the spectrum, which will be determined later. The exponent q is given by[6]

$$q = \frac{3\tau}{\tau - 1}, \qquad (6)$$

where the compression ratio τ is related to the Mach number $\mathcal{M}$ as

$$\frac{1}{\tau} = \frac{\gamma - 1}{\gamma + 1} + \frac{2}{\gamma + 1}\frac{1}{\mathcal{M}^2}. \qquad (7)$$

From the momentum distribution (5), and from the energy–momentum relation

$$p = m_e c \times \sqrt{\left(1 + \frac{E}{m_e c^2}\right)^2 - 1}, \qquad (8)$$

---

[5] Only the radial component is non-zero due to adopted spherical symmetry.

[6] Here, we neglect the Alfvén speed, with which the scattering centers presumably move, in comparison to the flow speed. This correction is only important for low Mach number shocks. Because synchrotron emission mainly comes from strong shocks, neglecting Alfvén speed will not change the spectrum significantly (e.g., Caprioli et al. 2009).

where E and m_e are the kinetic energy and the rest mass of electrons, respectively, and c is the speed of light. We can express the energy spectrum of the non-thermal electrons as

$$N_0(E) = 4\pi \mathcal{C}_0\, p^{2-q} \frac{dp}{dE}. \tag{9}$$

The energy of non-thermal electrons ranges between $E_{\rm min}$ (with the corresponding minimum momentum $p_{\rm min}$) and $E_{\rm max}$ (with maximum momentum $p_{\rm max}$). Following what is done in the computations of SNRs and galaxy clusters (e.g., Berezhko & Ellison 1999; Enßlin et al. 2007), the minimum momentum $p_{\rm min}$ is related to the downstream temperature T_2 by the injection parameter $x_{\rm inj}$:

$$p_{\rm min} = x_{\rm inj} \sqrt{2 \times m_e k_B T_2} \quad \text{(cgs)}. \tag{10}$$

For electrons, the maximum energy at the shock is determined by the balance between radiative loss and acceleration gain, which gives[7] (e.g., Webb et al. 1984; Reynolds 2008):

$$\begin{aligned} E_{\rm max} &= 71.65\,(u_s/10^8) \times (B_2/10^{-6})^{-0.5}\ \text{erg (cgs)} \\ &= 44.72\, u_{s,10^3\ \rm km\,s^{-1}} \times (B_{2,\mu\rm G})^{-0.5}\ \text{TeV}. \end{aligned} \tag{11}$$

where B_2 is the downstream magnetic field. Actually, in the test particle theory, the synchrotron spectrum is not very sensitive to the maximum energy $E_{\rm max}$. But the cutoff of the power-law spectrum does depend on $E_{\rm max}$. In order to determine the normalization of the electron spectrum, we follow the approach adopted in simulations of galaxy clusters (e.g., Enßlin et al. 2007; Pfrommer et al. 2008) and smoothly connect the power-law momentum spectrum of electrons to the downstream thermal spectrum at the momentum $p_{\rm min}$. Then the coefficient $\mathcal{C}_0$ in Equation (5) is given by

$$\mathcal{C}_0 = \frac{n_{e,2}}{(2\pi m_e k_B T_2)^{3/2}}\, p_{\rm min}^q\, e^{-p_{\rm min}^2/(2m_e k_B T_2)}, \tag{12}$$

where $n_{e,2}$ is the downstream electron number density.

The test particle result is valid only when the energy density of the non-thermal particles is small enough compared to the thermal energy density so that the CRs do not significantly change the structure of the shock. However, for a strong shock with a very high Mach number (e.g., when the shock encounters the cold shell), calculation with the above method will easily produce an electron energy density comparable to the downstream thermal energy. So in our calculations we have to choose appropriate normalization of the electron momentum spectrum for different Mach numbers, and we adopt the method used in Enßlin et al. (2007) and Pfrommer et al. (2008). First, we obtain the electron energy spectrum from Equations (9) and (12), so that the energy density of the non-thermal electrons $K_{e,0}$ is

$$K_{e,0} = \int_{E_{\rm min}}^{E_{\rm max}} E N_0(E) dE. \tag{13}$$

Then, the ratio between the non-thermal electron energy density and the downstream thermal energy density (in the test particle theory approach) is

$$\xi_{\rm lin} = \frac{K_{e,0}}{1.5 n_2 k_B T_2}, \tag{14}$$

where n_2 is the downstream total number density. The ratio $\xi_{\rm lin}$ can be very large for a shock with large $\mathcal{M}$. Now we set a maximum ratio between the non-thermal electron energy density and the downstream thermal energy density to $\xi_{\rm max} = 0.05$ (a value suggested by the simulations of Keshet et al. 2003; also see Pfrommer et al. 2008) and define a parameter $\chi \equiv \xi_{\rm lin}/\xi_{\rm max}$. The modified normalization of the electron momentum spectrum we use in our calculation becomes

$$\mathcal{C} = (1 - e^{-\chi})\chi^{-1}\, \mathcal{C}_0, \tag{15}$$

so that $\mathcal{C} \to \mathcal{C}_0$ for $\chi \to 0$, while $\mathcal{C} \to \mathcal{C}_0/\chi$ for very large values of χ. In other words, if $\xi_{\rm lin}$ is very small compared with $\xi_{\rm max}$ ($\chi \ll 1$), then $\mathcal{C} \sim \mathcal{C}_0$ and the energy density ratio is approximately $\xi_{\rm lin}$. However, if $\xi_{\rm lin}$ is very large compared with $\xi_{\rm max}$ ($\chi \gg 1$), the final energy density ratio between the non-thermal electrons and the downstream thermal energy density cannot exceed $\xi_{\rm max}$. Roughly speaking, the modification is important when $\mathcal{M}$ is larger than 10. Therefore, Equation (9) becomes

$$N(E) = 4\pi \mathcal{C}\, p^{2-q} \frac{dp}{dE}, \tag{16}$$

and the energy density and number density of the non-thermal electrons are given by

$$K_e = \int_{E_{\rm min}}^{E_{\rm max}} E N(E) dE, \quad N_e = \int_{E_{\rm min}}^{E_{\rm max}} N(E) dE. \tag{17}$$

The final ratio between the non-thermal electron energy density and downstream thermal energy density ξ is the same as Equation (14) with $K_{e,0}$ replaced by K_e. In particular, the injection coefficient η, a parameter determining the acceleration efficiency modeled in the diffusive shock acceleration mechanism (e.g., Enßlin et al. 2007), is defined here to be

$$\eta \equiv \frac{N_e}{n_{e,2}}. \tag{18}$$

Another thing which must be emphasized is that here we do not give the energy density of the non-thermal protons, which is unnecessary for our purpose. By using test particle theory we are assuming non-modified shocks, and the CR energy density is less than 10% of thermal energy density by assumption.[8] This is only a first-order approximation and a first step to determine whether a more advanced model is merited.

2.3. The Spectrum after the Shocks

The test particle framework described above gives the energy spectrum of the non-thermal electrons at the shock, and we need to compute the evolution of the spectrum further downstream. For simplicity, we assume no diffusion in our calculation. This means that once the accelerated electrons are generated at the shock, they are frozen to the fluid elements. So, while the shock propagates outward, the non-thermal electrons are left behind and move with the fluid. These non-thermal electrons suffer radiative and adiabatic losses, and the electron energy spectrum will change with time. The changes of the electron energy and number density are well known (e.g., Reynolds 1998; Cassam-Chenaï et al. 2007). We will describe our numerical

---

[7] In a typical elliptical galaxy, the energy density of IR background and starlight is usually small compared with the downstream magnetic energy density. So we ignore the electrons' inverse Compton cooling here.

[8] Some observations show that in SNRs 10% of the mechanical energy of the explosion can be converted into CRs (e.g., Aharonian et al. 2004).

implementation of the spectral evolution formulae of Reynolds (1998). We assume that an electron with energy E_0 is generated at time t_0 at radius r_0, where the mass density is ρ_0. At a later time t, the electron moves to the new position r, where the mass density is $\rho_t = \rho(r, t)$, so that the compression ratio of the fluid element is

$$\alpha(r, t) \equiv \frac{\rho_t}{\rho_0}. \quad (19)$$

After the losses, the energy of the electron at time t and radius r is

$$E(r, t) = \alpha^{1/3} \frac{E_0}{1 + \Theta E_0}, \quad (20)$$

where the quantity Θ is the result of the following integral

$$\Theta(t) \equiv \mathcal{A} \int_{t_0}^{t} B_{\rm eff}^2(t) \alpha^{1/3}(t) dt. \quad (21)$$

The coefficient in front of the integral is $\mathcal{A} \equiv 4e^4/(9m_e^4c^7) = 1.57 \times 10^{-3}$ (cgs; e is the electron's charge) and

$$B_{\rm eff} \equiv \sqrt{B^2 + B_{\rm cbr}^2(1+z)^4}, \quad (22)$$

where $B_{\rm cbr} \equiv 3.27\ \mu$G is the magnetic field strength with energy density equal to that of the cosmic microwave background at the redshift $z = 0$.

Each of the non-thermal electrons generated by the shock will change its initial energy according to the above equations, and the energy spectrum of these electrons when they are generated is given by the test particle result (Equation (16)). As the number of electrons is conserved, at time t and radius r the energy spectrum of these electrons becomes

$$N(E)_{r,t} = N(E_0)\alpha^{-2/3}\left[\frac{E_0(E)}{E}\right]^2. \quad (23)$$

Note that E_0 as a function of E is determined by inverting Equation (20). In particular, initially the maximum energy and minimum energy of the electrons are $E_{\rm max,0}$ and $E_{\rm min,0}$. Subsequently, the maximum energy and the minimum energy will also change to the new maximum energy $E_{\rm max}$ and the minimum energy $E_{\rm min}$ according to Equation (20).

Once we obtain the energy spectrum of the electrons, we can calculate the resulting synchrotron spectrum, i.e., the emissivity of the population of electrons in the energy interval $E_{\rm min} \leqslant E \leqslant E_{\rm max}$

$$J_\nu = \int_{E_{\rm min}}^{E_{\rm max}} \mathcal{P}(\nu)\, N(E) dE \quad \text{erg s}^{-1}\,\text{cm}^{-3}\,\text{Hz}^{-1}. \quad (24)$$

Then the luminosity L_ν can be calculated by integration of J_ν over the whole volume. In the above equation, the synchrotron emission from a single electron is given by

$$\mathcal{P}(\nu) = \frac{\sqrt{3}e^3 B_\perp}{m_e c^2} \frac{\nu}{\nu_c} \int_{\nu/\nu_c}^{\infty} K_{5/3}(x) dx \ \text{erg s}^{-1}\,\text{Hz}^{-1}, \quad (25)$$

where $K_{5/3}(x)$ is a modified Bessel function of the second kind, and

$$\nu_c = \frac{3eB_\perp}{4\pi m_e^3 c^5} E^2 \quad (26)$$

is the critical frequency, where E is the energy of the electron and $B_\perp$ is the magnetic field component perpendicular to the line of sight (e.g., Blumenthal & Gould 1970; Lazendic et al. 2004). In our calculation, $B_\perp$ is approximated by B given in Equation (4).

2.4. Numerical Method

As the shock emerges from the center of our model elliptical galaxy and moves outward, it will accelerate particles at each position it passes through. Once the non-thermal particles are generated by the shock, they will be frozen in the fluid element as we assume no diffusion, and the spectrum will evolve according to Equation (23). In practice, in our modeling, at every given time, there will be non-thermal electrons within a certain radial range with the new ones produced by the shock and the old ones moving out with the fluid. Accordingly, we calculate the synchrotron emissivity from Equation (24) at each radius and then obtain the total luminosity by integrating over the volume.

In practice, once the electrons are generated by a shock at certain radius r_0 at time t_0, we follow the fluid element and compute its position r_t at time t. From the hydrodynamic code, we know the velocity $v_r(t)$ and acceleration $a_r(t)$ of each fluid element, so that the new position r_t can be estimated as

$$r_t = r_0 + \sum_{t_0}^{t} \triangle r, \quad (27)$$

where the position increment $\triangle r$ in each time step $\triangle t$ is calculated as

$$\triangle r = v_r(t) \times \triangle t + \frac{1}{2} a_r(t) \times \triangle t^2. \quad (28)$$

For higher numerical accuracy, the quantities $v_r(t)$ and $a_r(t)$ of the fluid element at radius r could be approximated by the average velocity and acceleration of the two fluid elements at radius r and r+dr, which are given in the output from the code.

So, in our calculation, when a shock is found at time t, its position is determined by the criterion given in Equation (1). Then we follow the fluid element, that at time t was at the position of the shock according to Equations (27) and (28). After one time step, we identify the new position of the shock and follow a new fluid element. While following each fluid element that passed the shock, we calculate the value of $\Theta(t)$ given by Equation (21). In this way, we know the energy spectrum of the electrons from Equation (23) at different positions at time t, and we finally calculate the total synchrotron spectrum. Note that our numerical method is different from the standard method which solves the continuity equation for electrons in the two-dimensional phase space at each time step (e.g., Longair 1994). Instead, in our method, the energy spectrum at each time step is calculated analytically according to Equation (23), and we only need to follow the one-dimensional fluid element, which is computationally more efficient.

3. RESULTS FROM ONE SHOCK

Now we give an example of the determination of the properties of the synchrotron spectrum for a shock in model B3$_{02}$. In particular, we focus on the last major burst in the example described in Section 2.1.

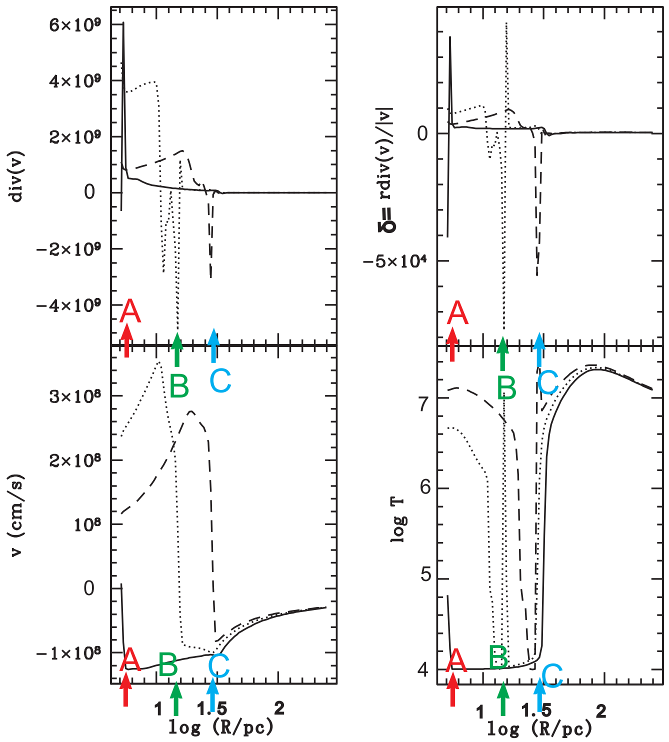

Figure 4. Shock-locating method. In the two top panels, the dimensional quantity div($\mathbf{v}$) (left panel) and the dimensionless function δ (right panel; Equation (1)) are shown for the same profiles shown in Figure 3. The solid, dotted, and dashed lines are in time order, separated by 0.004 Myr. The solid line is at time $\Delta t_1 = 0.235$ Myr after the time zero point. The three lines also show the movement of the shock, which can be used to estimate the shock velocity. There are three arrows and letters in the figure to show the position of shock found at different times.

(A color version of this figure is available in the online journal.)

3.1. *Synchrotron Spectrum*

We define the time when the SMBH bolometric accretion luminosity $L_{\rm BH}$ reaches 1% of Eddington luminosity $L_{\rm Edd}$ as the zero time point, corresponding to 6.48 Gyr in the code. Before the shock is formed and can be recognized by the code, a cold shell is falling toward the center, which can be seen clearly from Figure 2. From Figure 3, we can see that at a later time $\Delta t = 0.235$ Myr, the radial velocity changes from negative to positive, indicating the emergence of the nuclear wind and the shock. The result of Equation (1) is shown in Figure 4. At the position of the shock, the parameter δ has a minimum value, which confirms our criterion for finding the shock.

At each time, we find the position of the shock and follow the shock until it disappears. Meanwhile, we calculate the energy spectrum of the non-thermal electrons accelerated by the shock with Equation (16) and the spectral evolution according to Equation (23). Then the synchrotron emissivity at each radius is calculated from Equation (24) and the total synchrotron spectrum for our model elliptical galaxy is the sum of the emission from different positions. So, the final spectrum is actually not from a single population of power-law electrons, but from electrons at different times in their evolution. In Figure 5, we show the radial profile of the magnetic field, the non-thermal electron energy density and the flux for different frequencies at the time $\Delta t = 0.335$ Myr. The magnetic field is estimated according to Equation (4). At this time, the shock is located at about 327 pc and the bump of the magnetic field is due to the compression at the shock. The non-thermal electron energy density is estimated according to Equation (17). As we assume no diffusion, non-thermal electrons only exist in the radial region 258–327 pc at this time. The non-thermal electrons around 260 pc come from the initial strong shock (arrow A in Figure 4). The flux at radius R is estimated by $\nu J_\nu \times R$, and the fluxes of

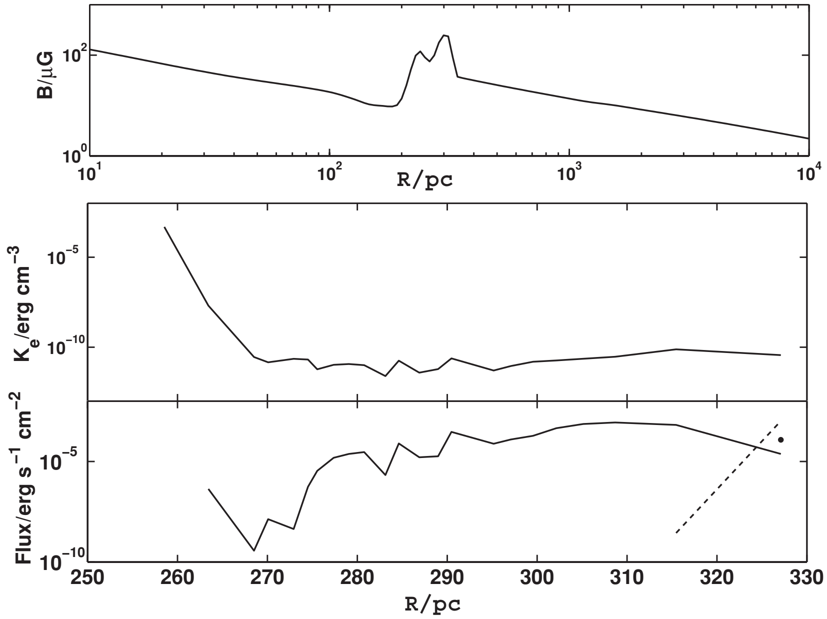

Figure 5. Radial profile of the magnetic field, electron energy density, and synchrotron flux for three frequencies at time $\Delta t = 0.335$ Myr. At this time, the shock is located at about 327 pc. The upper panel shows the radial profile of magnetic field estimated according to Equation (4) at this time. The bump around 300 pc is due to the compression by the shock. The middle panel shows the radial profile of electron energy density calculated according to Equation (17). As we assume no diffusion, non-thermal electrons only exist in the radial region 258–327 pc at this time. The lower panel shows the radial profile of the flux for different frequencies: radio band 4.84 GHz (solid line), optical band 7.25×10^{14} Hz (dashed line), and X-ray band 2.42×10^{17} Hz (the dot). The flux at radius R is estimated by $\nu J_\nu \times R$. Note that the higher the frequency is, the closer the flux is to the shock. At this time, the X-ray emission can only be found just after the shock, while the optical emission can be found in two cells after the shock. For the radio emission, it exists in a much more extended region.

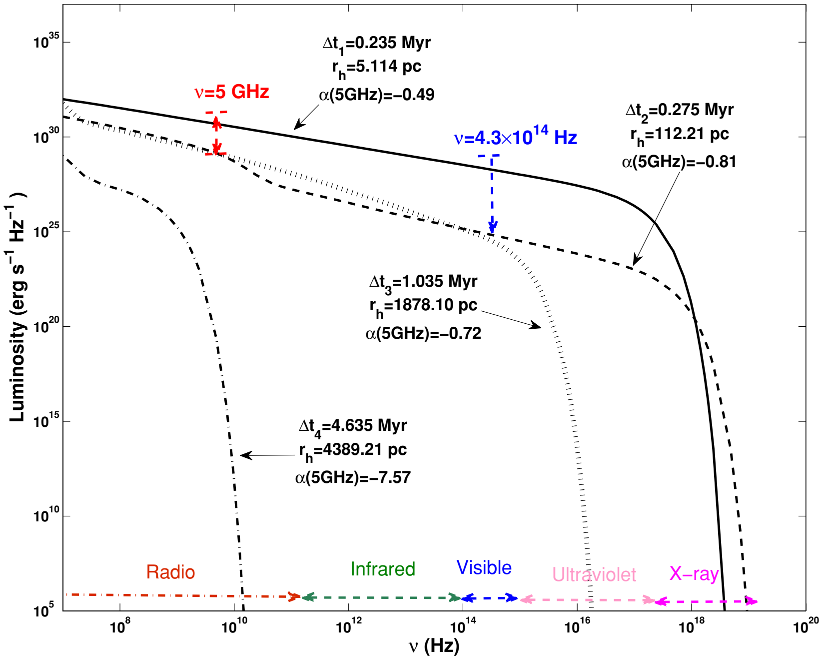

Figure 6. Synchrotron emission spectra without absorption at four different times. The solid, dashed, dotted, and dash-dotted lines are the total synchrotron spectrum from the elliptical galaxy at the time $\Delta t_1 = 0.235$ Myr, $\Delta t_2 = 0.275$ Myr, $\Delta t_3 = 1.035$ Myr, and $\Delta t_4 = 4.635$ Myr, respectively, after the defined time zero. The half radius r_h with each line is the radius within which half energy at the frequency 5 GHz is emitted. α is the spectral index defined in Equation (30). The arrow labeled with "$\nu = 5$ GHz" is the range of observed core radio luminosity at 5 GHz in FR-II sources (Zirbel & Baum 1995; Chiaberge et al. 2000). The arrow labeled with "$\nu = 4.3 \times 10^{14}$ Hz" is the range of observed core optical luminosities at 4.3×10^{14} Hz (wavelength $\lambda = 7000$ Å) in FR-II sources by *Hubble Space Telescope*, which are believed to originate from non-thermal emission (Chiaberge et al. 2000). At the bottom of this figure, the names for different frequency bands are labeled.

(A color version of this figure is available in the online journal.)

radio emission (4.84 GHz), optical emission (7.25×10^{14} GHz), and X-ray emission (2.42×10^{17} GHz) are labeled by solid line, dashed line, and a dot, respectively. Though the electron energy density around 260 pc is large, these are "old" electrons that do not contribute to the synchrotron emission in the three frequencies by this time. The X-ray emission can only be found just behind the shock, while the optical emission can be found within two cells of the shock. However, the radio emission can extend over almost the whole region passed by the shock.

In our model, the only free parameters needed to calculate the synchrotron emission are $x_{\rm inj}$, defined in Equation (10), which is related to the minimum momentum of the accelerated electrons, and the saturation parameter $\xi_{\rm max} = 0.05$. Here, we just take the value[9] $x_{\rm inj} = 3.6$, the same as the value taken in the model of Enßlin et al. (2007). Although the value $x_{\rm inj} = 3.6$ is used for protons in Enßlin et al. (2007), using the same $x_{\rm inj}$ for electrons results in the number ratio of relativistic electrons to protons at energies larger than 1 GeV to be about 10^{-2}, which can be seen from Equation (12). This is consistent with the ratio found in the local Galactic CRs and in the leptonic models of high-energy emission from SNRs (e.g., Zirakashvili & Aharonian 2010). Actually, the same value of $x_{\rm inj}$ is also used for electrons in Pfrommer et al. (2008). Effectively, for strong shocks, we increase $x_{\rm inj}$ to limit the total energy of non-thermal electrons. Note that as we do not include the jet feedback in the hydrodynamic simulation (see Paper I), the synchrotron emission calculated here is not the total emission that would be observed from a real elliptical galaxy. It can only be compared to elliptical galaxies without jets or to the core emission in elliptical galaxies with extended jets. We take snapshots at four different times during the evolution of the model. The resulting spectra are shown in Figure 6. The change of spectral shape with time in this figure is due to the radiative and adiabatic losses. In particular, the high frequency part disappears at late times (due to a smaller magnetic field at larger radii and losses). We define the fiducial radius r_h enclosing the volume within which half the energy at the frequency 5 GHz is emitted. The spectral index α at a certain frequency is defined to be the index of the power-law approximation:

$$J_\nu \propto \nu^\alpha. \tag{29}$$

In practice, we calculate the spectral index by the following difference:

$$\alpha = \frac{\log J_{\nu_1} - \log J_{\nu_2}}{\log \nu_1 - \log \nu_2}, \tag{30}$$

where the two frequencies are chosen to be $\nu_1 = 0.17$ GHz and $\nu_2 = 5$ GHz, so that we can compare our calculation with observations in the two bands. From Figure 6, we can see that the spectrum becomes steeper with time and the absolute value of the spectral index becomes larger. The ratio ξ of the non-thermal electron energy density generated by the shock to the downstream thermal energy density will change for different Mach numbers, as shown in Figure 7. The non-thermal electron energy density is calculated according to Equation (17). Note that the maximum ratio is $\xi \sim 0.05$, which is nearly reached only for very high Mach numbers. For small Mach numbers, the ratio is only about 0.001. Roughly speaking, when $\mathcal{M}$ is larger than 10, the saturation condition (Equation (15)) becomes very

---

[9] In the non-saturation limit, if $x_{\rm inj}$ is smaller, more electrons will be accelerated and the emission will be stronger while the contrary is also true. However, as electrons with momentum around $p_{\rm min}$ do not contain most of the energy for non-thermal electrons in strong shocks, the total spectrum is not very sensitive to $x_{\rm inj}$. In the saturation limit, $x_{\rm inj}$ is irrelevant because $\xi_{\rm max}$ controls the normalization.

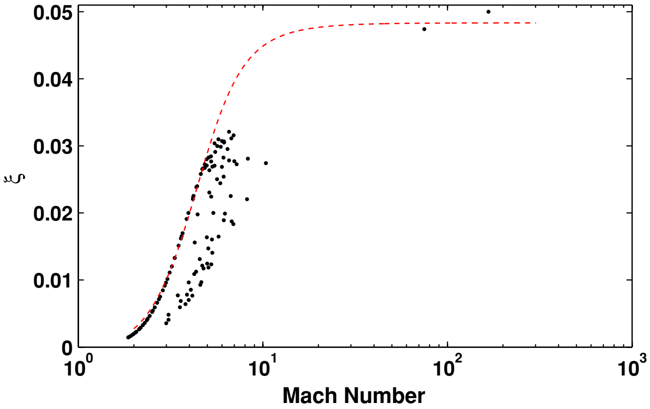

Figure 7. Acceleration efficiency at different Mach numbers, $\mathcal{M}$. The figure shows the ratio between the non-thermal electron energy density accelerated by the shock to the downstream thermal energy density just after the shock ξ, as computed from the hydrodynamic code. For high $\mathcal{M}$, the ratio is almost 0.05, which occurs when the shock encounters the cold shell. For small $\mathcal{M}$, the ratio can be around 0.001. To the degree that $\xi \ll 1$, the test particle theory adopted in this paper is accurate. Roughly speaking, when $\mathcal{M}$ is larger than 10, modification to the normalization (Equation (15)) is important. The red dashed line is the theoretical result of the model with an assumed constant downstream temperature 5×10^7 K, an assumed constant downstream number density 10 cm^{-3}, and an assumed maximum electron energy 100 TeV. Even for the same $\mathcal{M}$, the ratio ξ can be different for different temperature and number density.

(A color version of this figure is available in the online journal.)

important. Though we do not consider protons here, they will also be accelerated by the shock. As total CR energy density is estimated to be around 10% of the shock's kinetic energy (e.g., Aharonian et al. 2004), the energy density ratio between the protons and electrons will also change with Mach number. The adopted test particle theory assumes that the postshock CR pressure is small compared to the thermal gas pressure, and we find this assumption to be valid during most of the time of evolution except when the shock encounters the cold shell, where the modified spectrum takes effect. To the first order of approximation, we neglect the pressure of CRs, which is a first step to determine whether a more advanced model is merited.

3.2. *Synchrotron Radio Emission*

While the shock moves outward, it dissipates energy into the ISM and finally disappears. In this example, we can still see the shock at the time $\Delta t = 46$ Myr at the radius 32.7 kpc, where a second shock due to the next sub-burst emerges. But as we have shown in Figure 6, the radio emission is already almost unobservable at the time $\Delta t = 4.635$ Myr. In Figure 8, we show the evolution of the synchrotron emission size r_h (at 5 GHz, defined as the spatial radius enclosing half of the emitted synchrotron luminosity at the given time). Generally, r_h increases with time as the non-thermal electrons, which are frozen in the fluid elements, move outward. However, when the shock propagates into the regions with low magnetic field strength, there will be almost no synchrotron radio emission at 5 GHz and the apparent size will decrease at that time. The size r_h may change from a very small initial size (5.1 pc in this example) to around 4.5 kpc. In Figure 9, we show the evolution of synchrotron luminosity at four different frequencies. Note that the spectrum shown in Figure 6 is the emission spectrum without allowance for absorption. However, for radio bands, the optical depth due to synchrotron self-absorption at 0.1 GHz initially is only about 10^{-4} and smaller at later times. The synchrotron self-absorption is thus only important for frequencies smaller than 10^7 Hz in this example.

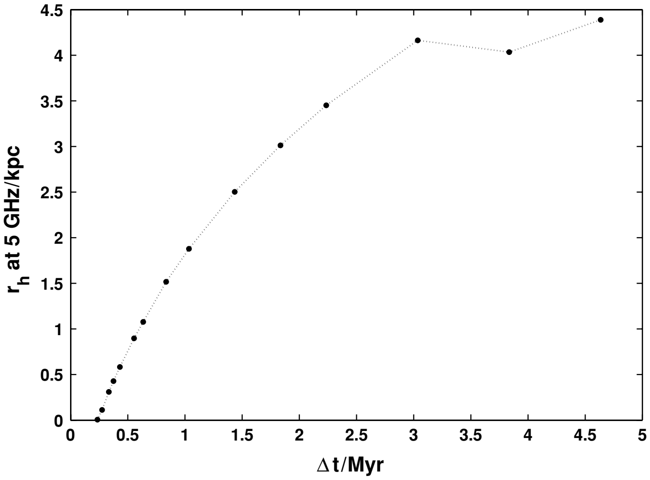

Figure 8. Evolution of the synchrotron radio emission size at 5 GHz. The size r_h is defined to be the radius within which half the energy at the frequency 5 GHz is emitted. At around 3 Myr, the size decreases because at this time there is no contribution to the 5 GHz synchrotron radio emission from the new shock position due to small magnetic field. Then the emission at this band is only from the "old" electrons, which suffer large radiation and adiabatic losses and move outward.

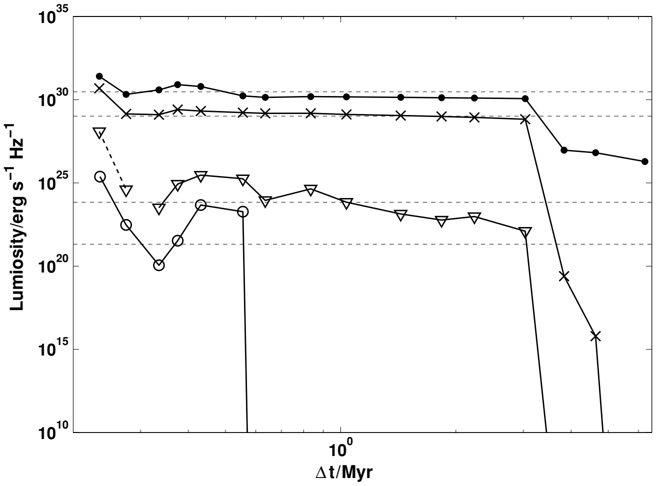

Figure 9. Evolution of the synchrotron luminosity in four different bands: $\nu =$ 0.17 GHz (solid dots, radio), $\nu = 4.84$ GHz (crosses, radio), $\nu = 7.25 \times 10^5$ GHz (triangle, optical, and the first two points in this line are connected by a dashed line because they will be absorbed by the dust), $\nu = 2.42 \times 10^8$ GHz (open circles, X-ray). The larger the frequency is, the sooner radiation at that frequency disappears. In the four horizontal dashed lines, we show what would be seen if νL_ν for each cited frequency band had the power 5×10^{38} erg s^{-1}.

3.3. *Synchrotron Emission in Other Bands*

For optical bands, the main absorption is due to dust. The optical depth due to dust absorption is calculated in the code (Paper I). The optical emission is absorbed by dust for $\Delta t \leqslant$ 0.33 Myr (within 300 pc in this example), but the absorption is not important after that time. A fiducial estimate of the expected mean flux Σ_o of the optical synchrotron emission is obtained as $\Sigma_o \equiv L_o/(2\pi r_{h,o}^2)$, where L_o is the total synchrotron luminosity in the optical band (7.25×10^{14} Hz), and where we have neglected the difference between the radius within which half of luminosity is emitted $r_{h,o}$ and the projected surface effective radius. We compare Σ_o with the optical flux of our galaxy model, to see whether the synchrotron optical emission can be observed or not. In order to estimate the stellar flux of the galaxy model, we adopt as a fiducial value for the surface brightness at the effective radius $\Sigma_e = 22$ mag arcsec^{-2}, and for the effective

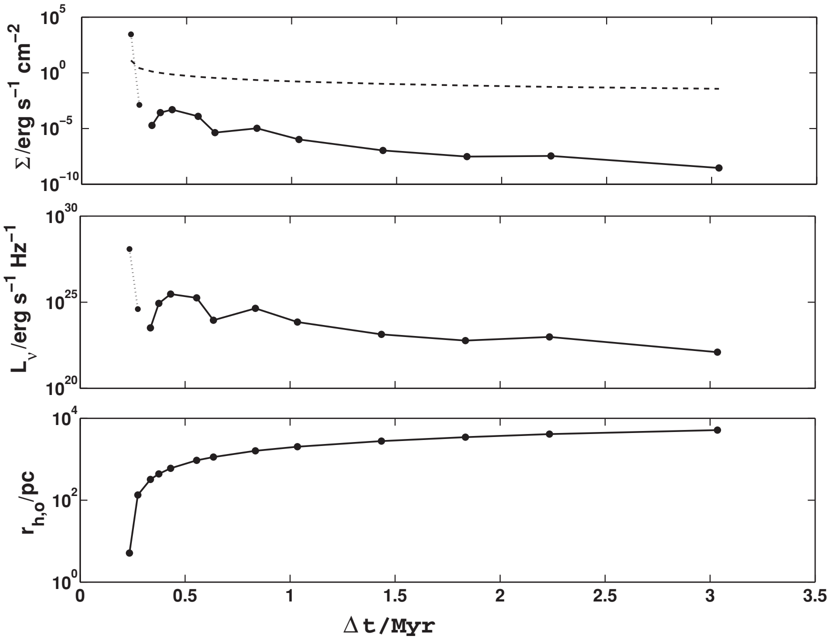

Figure 10. Properties of synchrotron (optical) emission in model B3$_{02}$. This figure shows the time evolution of the flux Σ (upper panel), luminosity L_ν (middle panel), and size $r_{h,o}$ (lower panel) at the frequency 7.25×10^{14} Hz. The dashed line in the top panel is $\Sigma_\star(r_{h,o}/R_e)$, i.e., the stellar flux of a de Vaucouleurs profile with $\Sigma_e = 22$ mag arcsec^{-2} and $R_e = 6.9$ kpc. In the upper and middle panels, the first two points are connected by dotted lines because the optical emission will be absorbed by dust at that time. Note that synchrotron emission lasts for 2.8 Myr and then drops to zero very quickly.

radius $R_e = 6.9$ kpc. At each time, we then compare the value of Σ_o with the stellar flux profile obtained from the de Vaucouleurs profile, i.e., with $\Sigma_\star(r_{h,o}/R_e)$. The result is shown in Figure 10. This figure shows that the synchrotron optical emission is stronger than the starlight only at early times. Later on, it is too faint compared with the starlight. However, the optical emission will be absorbed by the dust in this example at the early time. So we expect to observe synchrotron optical emission at the inner part of those elliptical galaxies with little dust during a short time in the quasar phase. This result is just from one shock at the first sub-burst of the last major burst in Figure 1. However, we stress that within each burst several shocks appear from the sub-bursts in the galaxy almost simultaneously, which will give stronger emission and a higher probability of observing the synchrotron optical emission. The study of the cumulative effect of several co-existing shocks is beyond the reach of the present investigation, and it is postponed to a future work. In particular, it will also be important to consider the more realistic case of multiple shocks created by the so-called "time-dependent nuclear wind treatment" which includes the time for the wind to reach different radii (see Paper I; also see Section 4). Right now, we have just checked that, for a single shock, the time-dependent and time-independent wind (neglecting the time needed for the wind to reach different radii) models do produce very similar results.

Figure 6 shows that there is also synchrotron X-ray emission for the duration of $\sim 10^4$ yr to $\sim 10^5$ yr at the very early time of the burst. At the time $\Delta t = 0.235$ Myr, at the frequency 2.4×10^{17} Hz (equivalent to 1 keV), the luminosity is 5.76×10^{42} erg s^{-1} while at the frequency 1.2×10^{18} Hz (equivalent to 5 keV), the luminosity is 1.2×10^{38} erg s^{-1}. The synchrotron X-ray emission lasts for only 0.32 Myr and rapidly drops to zero after that time. Time evolution of the flux, luminosity, and size for soft X-ray synchrotron emission is shown in Figure 11. Typically, the luminosity of the thermal X-ray emission in the band 0.5–2.0 keV from isolated elliptical galaxies varies from 10^{39} to 10^{41} erg s^{-1} (e.g., Memola et al. 2009). So the synchrotron X-ray emission are likely to be observed only in these "on" state galaxies, which are only a small fraction of all galaxies. Because the spectrum of bremsstrahlung emission (energy density per Hz) is almost flat, we should expect the luminosity of bremsstrahlung optical emission to be around 10^{35}–10^{37} erg s^{-1} based on the bremsstrahlung X-ray emission. This is actually smaller than the synchrotron optical emission here.

As synchrotron X-ray emission is also observed from SNRs, we can scale down the flux of the X-rays calculated here to a typical flux of X-rays from SNRs. If synchrotron emission from SNRs and elliptical galaxies is from the same mechanism and we keep the ratio of synchrotron optical emission and synchrotron X-ray emission calculated here, we can estimate the flux of synchrotron optical emission from SNRs and see if it can be observed. Because the synchrotron spectrum basically becomes steeper with time, we can use the ratio at the initial time to estimate the lower bound of the synchrotron optical emission from SNRs. The synchrotron X-ray flux observed from SNR G330.2+1.0 is about 10^{-11} erg s^{-1} cm^{-2} (Park et al. 2009). In our calculation, at the time $\Delta t = 0.235$ Myr (see the solid line in Figure 6), the X-ray flux (at 1 keV) is about 1.85×10^3 erg s^{-1} cm^{-2} while the optical flux is about 2.83×10^3 erg s^{-1} cm^{-2}. Then we give a lower bound of synchrotron optical emission from SNRs to be 1.53×10^{-11} erg s^{-1} cm^{-2}, corresponding to 44.87 mag arcsec^{-2} without absorption. Actually, in SNR G332.5−5.6, line emission with a flux as faint as 10^{-12} erg s^{-1} cm^{-2} has been observed (Stupar et al. 2007). It seems that the synchrotron optical emission from SNRs should be observable by the appropriate technique.

4. DISCUSSION

4.1. Observational Consequences of Our Model

Our model has observational predictions, some of which are consistent with current radio observations and some of which

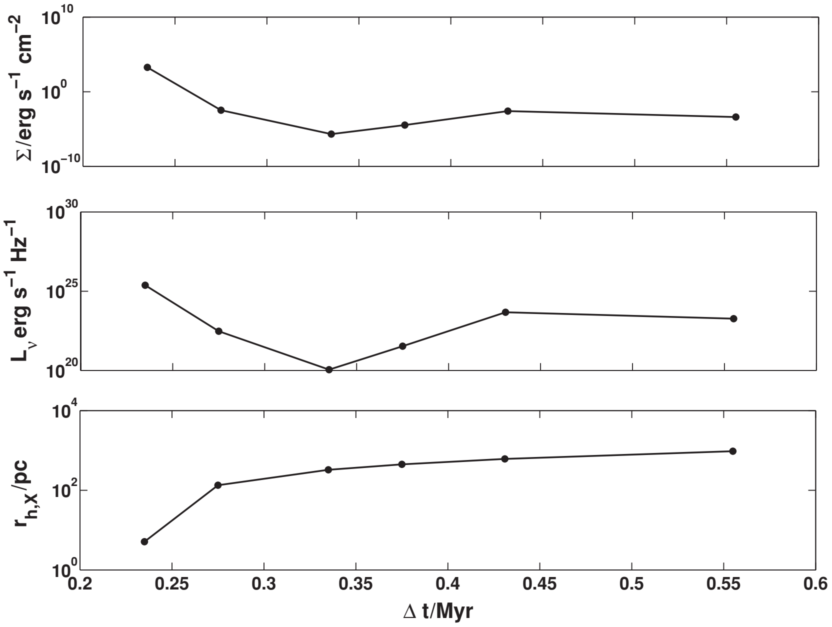

Figure 11. Properties of the synchrotron (soft X-ray) emission in model $B3_{02}$. This figure shows the time evolution of the flux Σ (upper panel), luminosity L_ν (middle panel), and size $r_{h,x}$ (lower panel) at the frequency 2.41×10^{17} Hz at different times. The half radius in the X-ray band is almost the same as the radius of the shock, which means the synchrotron X-ray emission only exists within a narrow region around the shock.

may be feasible *Chandra* source detections. First, as shown in Figure 6, the synchrotron emission at 5 GHz and 4.3×10^{14} Hz falls in the range of observed values in FR-II sources, which means that our mechanism should not be neglected. Besides, recent observations at 1.4 GHz find some early-type core galaxies hosting radio-loud AGN of extremely low radio power (Baldi & Capetti 2009), which can be interpreted as radio emission via the mechanism described here as it would be too weak to be produced by typical jets. Second, as shown in Figure 8, the shocks produced in the simulations easily reach the kiloparsec scale before they die away gradually. The synchrotron radio emission can also go to this large scale (though it is very weak). Actually, kiloparsec-scale outflows or winds have been observed in high redshift quasars (e.g., de Kool et al. 2001; Nesvadba et al. 2008; Nesvadba 2009; Cattaneo et al. 2009), which provides strong support for our scenario based on the computed winds in the AGN simulations. In particular, a recent observation (Alexander et al. 2010) finds a galaxy-wide outflow at redshift ∼2, which is believed to be a wind radiatively driven by the AGN and/or supernovae winds rather than by jets. Note that some observed X-shaped radio galaxies (e.g., Leahy & Williams 1984; Kraft et al. 2005; Saripalli et al. 2008) provide significant support for the idea that the observed radio emission arises from shocks caused by feedback from the SMBHs, as the broad-line winds drive shocks into the ambient gas with a similar shape (e.g., Drew & Proga 2000; Dorodnitsyn et al. 2008).

Third, the duration of synchrotron emission at a certain frequency will decrease with increasing frequency. For a single shock, synchrotron X-ray emission can only exist behind the shock, where the non-thermal electrons are just created. The synchrotron optical emission can extend to a larger region while the synchrotron radio emission can almost extend to the whole region where the shock has passed, which can be seen from Figure 5. So, in principle, at good enough resolution we should see the synchrotron emission in different bands at different spatial positions.

Though synchrotron emission from our mechanism and jets is similar to a certain extent, there are some differences that can help distinguish the two mechanisms. In the following, we list four possible observational tests. First, we expect the magnetic field in the shocked material to be more randomized than the magnetic field in the jets. So, the polarization of the emission from our mechanism will be weaker than the polarization of the emission from the jets, and polarization observations can help to disentangle the two mechanisms. Second, as the shock (and the synchrotron emission) is produced after each AGN outburst, emission from our mechanism will only exist in a certain fraction of elliptical galaxies, proportional to the duty cycle. In practice, in a survey of elliptical galaxies, where the emission from jets gives the background level of core radio emission, the number of galaxies with extra radio emission should be comparable to the duty cycle (see Paper I for a discussion of duty cycle of the models). Third, as the velocity of the jet is typically much larger than the velocity of the shock, then if we can directly measure the velocity of the outflow, it will be easy to tell which process dominates. Finally, the variability timescale of emission from jets is shorter than that of our mechanism. The variability timescale can also help us tell the origin of the core radio emission.

4.2. *Possible Future Improvements of the Model*

There are still some significant uncertainties in our model and further improvements are needed. First, the hydrodynamic code does not include the magnetic field, a fundamental ingredient for the accurate computation of synchrotron emission. In this paper, we only assumed a ratio between the magnetic pressure and the thermal pressure to estimate the preshock magnetic field in elliptical galaxies. A better method is needed to give the distribution of magnetic field and its evolution with time.

In fact, the magnetic field will be amplified near the shock due to back reaction of CRs, and we roughly estimate that the amplified magnetic pressure should not exceed about 10% of the postshock thermal pressure. A more careful calculation of this effect (e.g., Bell 2004; Riquelme & Spitkovsky 2009; Ohira et al. 2009; Zirakashvili & Ptuskin 2008) would be preferable. Second, we use the test particle theory to calculate the energy spectrum of the non-thermal electrons and neglect the modification of the shock structure due to the CRs. However, as is already known in SNRs, non-linear theory is needed to calculate the spectrum of the non-thermal electrons for strong shocks, especially at high energies (e.g., Berezhko & Ellison 1999; Lazendic et al. 2004; Lee et al. 2008; Treumann & Jaroschek 2008; Reynolds 2008). So in order to calculate the synchrotron emission more accurately, we will need to include the diffusive shock acceleration mechanism into the hydrodynamic code. This greatly adds to the complexity of the modeling. Third, as anticipated in Section 2.1, all the results presented here are obtained using a 1D code. Of course, this is quite a strong approximation, which precludes the quantitative analysis of several phenomena that almost certainly take place in real galaxies. One of the most important in the present context is the possible cold shell fragmentation due to Rayleigh–Taylor instability following central outburst. While we could not exclude this possibility, we note that several properties of our 1D models (such as the duty cycle, mass accreted on the central SMBH, star formation, X-ray luminosity) agree well with the observations, so that we are confident that the basic physics of feedback is actually captured by our simulations. Also note that on the kiloparsec scale, the central outbursts, even if initially anisotropic, will necessarily become rounder and rounder as they propagate, and therefore better and better approximated by our code.

The calculations here are based on the so-called "time-independent nuclear wind model" (with mechanical as well radiation feedback). In this simplified approach, which saves much simulation time, the propagation velocity of the wind along the numerical grid (Paper I, Equation (29)) is set to be infinity. Therefore, the nuclear wind mass, momentum, and kinetic energy are instantaneously discharged over the whole computational grid. The more realistic model is the time-dependent nuclear wind model, which will be more accurate, especially at the inner part of the galaxy at early times (Section 2.3 of Paper I). More accurate calculations of the synchrotron optical and X-ray emission also require the time-dependent wind model. Finally, effects of multiple shocks on the emission from the inner galaxy and on the re-acceleration of pre-existing non-thermal particles have yet to be included.

These caveats aside, the presented results show that central outbursts of mechanical and radiative energy consequent to AGN flaring should produce shock accelerated electrons capable of producing the non-thermal emission actually observed from the cores of some elliptical galaxies subsequent and consequent to AGN outbursts.

5. CONCLUSIONS

In this paper, we have explored the observational consequences of a new mechanism for producing the synchrotron emission seen in elliptical galaxies. This idea is based on particle acceleration subsequent to bursts of energy from the central black holes. The properties of the ISM are computed from hydrodynamic simulations including radiative and mechanical feedback consequent to an AGN outburst. Due to this feedback, a wind is formed during the quasar phases, and a shock is driven into the elliptical galaxy. Given standard physics, the shock, during its propagation into the galaxy, will accelerate electrons and protons via the diffusive shock acceleration mechanism. Synchrotron emission arises from these non-thermal electrons. In this paper, we have focused on the computation of the energy spectrum of the integrated synchrotron radiation. We include radiation loss and adiabatic loss during the evolution of these non-thermal electrons, and we show the change of the synchrotron spectrum with time.

In general, we have found that the synchrotron radio emission from one shock can last about 4.7 Myr at 5 GHz, while a shock can exist for 46 Myr. During the evolution of the elliptical galaxy, there are several major bursts and several sub-bursts for each major burst. Roughly speaking, the shock can exist during the whole burst phase of the galaxy while the radio emission (around 5 GHz) exists for 10% of the burst phase. Besides, our mechanism also gives marginally detectable synchrotron optical emission during the 3 Myr after a burst. The duration of synchrotron optical emission is about 50% of the radio emission at ∼0.17 GHz while the duration of the synchrotron X-ray emission is approximately 5% of the radio synchrotron emission at ∼0.17 GHz. The half radius of the synchrotron X-ray emission is almost the same as the radius of the shock, which means that the synchrotron X-ray emission only exists as a "ring" around the shock while the half radii of the synchrotron radio emission and synchrotron optical emission are smaller than the shock radius, which indicates that the synchrotron radio emission and the synchrotron optical emission are more diffuse. Actually, synchrotron optical emission from the cores of elliptical galaxies has been claimed to be observed by *Hubble Space Telescope* with a typical luminosity $\sim 10^{25}$–10^{29} erg s^{-1} Hz^{-1} (e.g., Chiaberge et al. 2000). The detection of synchrotron X-ray emission from elliptical galaxy cores is on the edge of currently feasible *Chandra* observations (e.g., Tananbaum 2001).

One point which needs to be emphasized is that the mechanism for synchrotron radio emission discussed here is different from that produced by jets. Current understanding of the AGN phenomena divides the activity into two phases: the "optical mode," immediately after the central outburst, and "radio mode" at low Eddington ratios between major outbursts, when powerful jets are emitted. In particular, here we have discussed the particle acceleration during the optical mode, which should exist for each quasar event associated with the outburst phase. Though the synchrotron radio emission from large scale jets may be stronger than the presented mechanism, our mechanism is also important for the synchrotron emission at the central part of elliptical galaxies and it could also be important for the evolution of the galaxy since the energy is released within the gaseous envelope of the galaxy. Definite observation of non-thermal emission from AGN hosting galaxy cores would strengthen the case for AGN feedback. Though there may be unresolved jets in the galaxy cores as pointed out by some observers (e.g., Ho 2008 and references therein), our mechanism contributes comparable emission to these small jets, if not larger.

Y.-F.J. thanks Carlos Badeness, John Hughes for suggestions on diffusive shock acceleration mechanisms, and Roberto Fanti, Luis Ho, Jenny Greene, Christoph Pfrommer, Aristotle Socrates, Yue Shen, Min-Su Shin, and Lorenzo Sironi for helpful discussions. We also thank two anonymous referees for comments that significantly improved the paper. Y.-F.J. thanks Princeton University for financial support. A.S. acknowledges support from NSF grant AST-0807381.

REFERENCES

Aharonian, F. A., et al. 2004, Nature, 432, 75
Alexander, D. M., Swinbank, A. M., Smail, I., McDermid, R., & Nesvadba, N. 2010, MNRAS, in press (arXiv:0911.0014)
Baldi, R. D., & Capetti, A. 2009, A&A, 508, 603
Bell, A. R. 2004, MNRAS, 353, 550
Berezhko, E. G., & Ellison, D. C. 1999, ApJ, 526, 385
Berezhko, E. G., & Völk, H. J. 2006, A&A, 451, 981
Best, P. N. 2007, New Astron. Rev., 51, 168
Blandford, R., & Eichler, D. 1987, Phys. Rep., 154, 1
Blandford, R. D., & Ostriker, J. P. 1978, ApJ, 221, L29
Blandford, R. D., & Rees, M. J. 1974, MNRAS, 169, 395
Blumenthal, G. R., & Gould, R. J. 1970, Rev. Mod. Phys., 42, 237
Bridle, A. H., & Perley, R. A. 1984, ARA&A, 22, 319
Burkert, A., & Silk, J. 2001, ApJ, 554, L151
Caprioli, D., Blasi, P., & Amato, E. 2009, MNRAS, 396, 2065
Cassam-Chenaï, G., Hughes, J. P., Ballet, J., & Decourchelle, A. 2007, ApJ, 665, 315
Cattaneo, A., et al. 2009, Nature, 460, 213
Chartas, G., et al. 2009, New Astron. Rev., 53, 128
Chiaberge, M., Capetti, A., & Celotti, A. 2000, A&A, 355, 873
Churazov, E., Forman, W., Vikhlinin, A., Tremaine, S., Gerhard, O., & Jones, C. 2008, MNRAS, 388, 1062
Ciotti, L., Morganti, L., & de Zeeuw, P. T. 2009a, MNRAS, 393, 491
Ciotti, L., & Ostriker, J. P. 1997, ApJ, 487, L105
Ciotti, L., & Ostriker, J. P. 2001, ApJ, 551, 131
Ciotti, L., & Ostriker, J. P. 2007, ApJ, 665, 1038
Ciotti, L., Ostriker, J. P., & Proga, D. 2009b, ApJ, 699, 89 (Paper I)
de Kool, M., Arav, N., Becker, R. H., Gregg, M. D., White, R. L., Laurent-Muehleisen, S. A., Price, T., & Korista, K. T. 2001, ApJ, 548, 609
Dickel, J. R., Sault, R., Arendt, R. G., Korista, K. T., & Matsui, Y. 1988, ApJ, 330, 254
Di Matteo, T., Springel, V., & Hernquist, L. 2005, Nature, 433, 604
Dorodnitsyn, A., Kallman, T., & Proga, D. 2008, ApJ, 675, L5
Drew, J. E., & Proga, D. 2000, New Astron. Rev., 44, 21
Ellison, D. C., Berezhko, E. G., & Baring, M. G. 2000, ApJ, 540, 292
Ellison, D. C., Decourchelle, A., & Ballet, J. 2004, A&A, 413, 189
Ellison, D. C., Patnaude, D. J., Slane, P., Blasi, P., & Gabici, S. 2007, ApJ, 661, 879
Enßlin, T. A., Pfrommer, C., Springel, V., & Jubelgas, M. 2007, A&A, 473, 41
Fabian, A. C. 1999, MNRAS, 308, L39
Ferrarese, L., & Merritt, D. 2000, ApJ, 539, L9
Field, G. B. 1965, ApJ, 142, 531
Fujita, Y., Kohri, K., Yamazaki, R., & Kino, M. 2007, ApJL, 663, L61
Gebhardt, K., et al. 2000, ApJ, 539, L13
Gilbert, G. M., Riley, J. M., Hardcastle, M. J., Croston, J. H., Pooley, G. G., & Alexander, P. 2004, MNRAS, 351, 845
Graham, A. W., & Driver, S. P. 2007, ApJ, 655, 77
Granato, G. L., De Zotti, G., Silva, L., Bressan, A., & Danese, L. 2004, ApJ, 600, 580
Hamann, F., Kaplan, K. F., Hidalgo, P. R., Prochaska, J. X., & Herbert-Fort, S. 2008, MNRAS, 391, L39
Ho, L. C. 2008, ARA&A, 46, 475
Hooper, E. J., Impey, C. D., Foltz, C. B., & Hewett, P. C. 1995, ApJ, 445, 62
Hopkins, P. F., Hernquist, L., Cox, T. J., Di Matteo, T., Robertson, B., & Springel, V. 2006, ApJS, 163, 1
Hu, J., Shen, Y., Lou, Y.-Q., & Zhang, S. 2006, MNRAS, 365, 345
Johansson, P. H., Naab, T., & Burkert, A. 2009, ApJ, 690, 802
Kellermann, K. I., Sramek, R. A., Schmidt, M., Green, R. F., & Shaffer, D. B. 1994, AJ, 108, 1163
Kembhaavi, A. K., & Narlikar, J. V. 1999, Quasars and Active Galactic Nuclei (Cambridge: Cambridge Univ. Press)
Keshet, U., Waxman, E., Loeb, A., Springel, V., & Hernquist, L. 2003, ApJ, 585, 128
King, A. 2003, ApJ, 596, L27
Kormendy, J., & Richstone, D. 1995, ARA&A, 33, 581
Koyama, K., Petre, R., Gotthelf, E. V., Hwang, U., Matsuura, M., Ozaki, M., & Holt, S. S. 1995, Nature, 378, 255
Kraft, R. P., Hardcastle, M. J., Worrall, D. M., & Murray, S. S. 2005, ApJ, 622, 149
Krolik, J. H. 1999, Active Galactic Nuclei: From the Central Black Hole to the Galactic Environment (Princeton: Princeton Univ. Press)
Lauer, T. R., et al. 2007, ApJ, 662, 808
Lazendic, J. S., Slane, P. O., Gaensler, B. M., Reynolds, S. P., Plucinsky, P. P., & Hughes, J. P. 2004, ApJ, 602, 271
Leahy, J. P., & Williams, A. G. 1984, MNRAS, 210, 929
Lee, S.-H., Kamae, T., & Ellison, D. C. 2008, ApJ, 686, 325
Longair, M. S. 1994, High Energy Astrophysics, Vol. 2 (Cambridge: Cambridge Univ. Press)
Lou, Y.-Q., & Jiang, Y.-F. 2008, MNRAS, 391, L44
Magorrian, J., et al. 1998, AJ, 115, 2285
Martel, A. R., et al. 1999, ApJS, 122, 81
McLure, R. J., & Dunlop, J. S. 2002, MNRAS, 331, 795
Memola, E., Trinchieri, G., Wolter, A., Focardi, P., & Kelm, B. 2009, A&A, 497, 359
Milosavljević, M., Couch, S. M., & Bromm, V. 2009, ApJ, 696, L146
Mirabel, I. F., & Rodríguez, L. F. 1999, ARA&A, 37, 409
Moe, M., Arav, N., Bautista, M. A., & Korista, K. T. 2009, ApJ, 706, 525
Mullin, L. M., Hardcastle, M. J., & Riley, J. M. 2006, MNRAS, 372, 113
Naab, T., Jesseit, R., & Burkert, A. 2006, MNRAS, 372, 839
Nesvadba, N. P. H. 2009, arXiv:0906.2900
Nesvadba, N. P. H., Lehnert, M. D., De Breuck, C., Gilbert, A. M., & van Breugel, W. 2008, A&A, 491, 407
Ohira, Y., Reville, B., Kirk, J. G., & Takahara, F. 2009, ApJ, 698, 445
Ostriker, J. P., Weaver, R., Yahil, A., & McCray, R. 1976, ApJ, 208, L61
Park, S., Kargaltsev, O., Pavlov, G. G., Mori, K., Slane, P. O., Hughes, J. P., Burrows, D. N., & Garmire, G. P. 2009, ApJ, 695, 431
Peterson, J. R., & Fabian, A. C. 2006, Phys. Rep., 427, 1
Pfrommer, C., Enßlin, T. A., & Springel, V. 2008, MNRAS, 385, 1211
Rees, M. J. 1971, Nature, 229, 312
Reynolds, S. P. 1998, ApJ, 493, 375
Reynolds, S. P. 2008, ARA&A, 46, 89
Riquelme, M. A., & Spitkovsky, A. 2009, ApJ, 694, 626
Saripalli, L., Subrahmanyan, R., Laskar, T., & Koekemoer, A. 2008, arXiv:0806.3518
Sazonov, S. Y., Ostriker, J. P., Ciotti, L., & Sunyaev, R. A. 2005, MNRAS, 358, 168
Sijacki, D., Springel, V., di Matteo, T., & Hernquist, L. 2007, MNRAS, 380, 877
Silk, J., & Rees, M. J. 1998, A&A, 331, L1
Sironi, L., & Socrates, A. 2010, ApJ, 710, 891
Springel, V., Di Matteo, T., & Hernquist, L. 2005, MNRAS, 361, 776
Stupar, M., Parker, Q. A., Filipović, M. D., Frew, D. J., Bojičić, I., & Aschenbach, B. 2007, MNRAS, 381, 377
Tananbaum, H. 2001, in ASP Conf. Proc., Vol. 234, X-ray Astronomy 2000, ed. R. Giacconi, S. Serio, & L. Stella (San Francisco, CA: ASP), 3
Tremaine, S., et al. 2002, ApJ, 574, 740
Treumann, R. A., & Jaroschek, C. H. 2008, arXiv:0806.4046
Wang, J.-M. 2008, ApJ, 682, L81
Webb, G. M., Drury, L. O., & Biermann, P. 1984, A&A, 137, 185
Zirakashvili, V. N., & Aharonian, F. A. 2010, ApJ, 708, 965
Zirakashvili, V. N., & Ptuskin, V. S. 2008, ApJ, 678, 939
Zirbel, E. L., & Baum, S. A. 1995, ApJ, 448, 521